

Pyrolysis of Covalent Organic Frameworks: A General Strategy for Template Converting Conventional Skeletons into Conducting Microporous Carbons for High-Performance Energy Storage

Qing Xu,^{a,b} Yanping Tang,^c Lipeng Zhai,^{a,b} Qihong Chen^a and Donglin Jiang^{a*}

^a *Field of Environment and Energy, School of Materials Science, Japan Advanced Institute of
Science and Technology, 1-1 Asahidai, Nomi 923-1292, Japan*

^b *Department of Structural Molecular Science, School of Physical Science, SOKENDAI
Hayama, Kannagawa 240-0193, Japan*

^c *School of Chemistry and Chemical Engineering, Shanghai Jiao Tong University, Shanghai
200240, P. R. China*

E-mail: djiang@jaist.ac.jp

Contents

Section A. Materials and Method

Section B. Supporting Figures

Section C. Supporting Tables

Section D. Supporting References

Section A. Materials and Method

Materials and Reagents. 4,4'-Sulfonyldiphenol (BPS) and triethylamine (TEA) were purchased from TCI. Hexachlorocyclotriphosphazene (HCCP) was purchased from Sigma-aldrich. Mesitylene, dioxane, tetrahydrofuran (THF), and acetonitrile were purchased from Wako Chemicals. Potassium hydroxide (KOH) was purchased from Kanto Chemicals.

Fourier transform infrared (FT IR) spectra were recorded on a JASCO model FT IR-6100 infrared spectrometer. Powder X-ray diffraction (PXRD) data were recorded on a Rigaku model RINT Ultima III diffractometer by depositing powder on glass substrate, from $2\theta = 1.5^\circ$ up to 60° with 0.02° increment. TGA measurements were performed on a Mettler-Toledo model TGA/SDTA851e under N_2 , by heating to $1000^\circ C$ at a rate of $10^\circ C \text{ min}^{-1}$. X-ray photoelectron spectroscopy (XPS) experiments were carried out on a AXIS Ultra DLD system from Kratos with Al $K\alpha$ radiation as X-ray source for radiation. Raman spectra were recorded on a SEN TERRA spectrometer (Bruker) employing a semiconductor laser ($\lambda = 532 \text{ nm}$). FE SEM images were obtained on a FEI Sirion-200 field-emission scanning electron microscope at an electric voltage of 10 KV. Supersonicated reactions were conducted by using an ultrasonic cleaning machine using Sharp UT-305HS. High resolution transmission electron microscopy (HRTEM) was conducted on a Hitachi H-7100 TEM at an electric voltage of 100 KV.

Computational Calculations. The crystalline structure of TAPT-DHTA-COF was determined using the density-functional tight-binding (DFTB+) method including Lennard-Jones (LJ) dispersion. The calculations were carried out with the DFTB+ program package version 1.2.^[S1] DFTB is an approximate density functional theory method based on the tight binding approach and utilizes an optimized minimal LCAO Slater-type all-valence basis set in combination with a two-center approximation for Hamiltonian matrix elements. The Coulombic interaction between partial atomic charges was determined using the self-

consistent charge (SCC) formalism. Lennard-Jones type dispersion was employed in all calculations to describe van der Waals (vdW) and π -stacking interactions. The lattice dimensions were optimized simultaneously with the geometry. Standard DFTB parameters for X–Y element pair (X, Y = C, O, H, and N) interactions were employed from the mio-0-1 set.^[S2]

Electrochemical Capacitance Measurements. Electrochemical characterizations were conducted on an EG & potentiostat/galvanostat Model 2273 advanced electrochemical system. A conventional cell with a three-electrode configuration was employed throughout this study. Working electrode was prepared by mixing resulting porous carbons with carbon black (Mitsubishi Chemicals, Inc.), and poly(vinyl difluoride) (PVDF) at a weight ratio of 85:10:5 and pasting the mixture on foaming nickel electrodes. A platinum foil was applied as a counter electrode with a Ag/AgCl reference electrode. The experiments were carried out in 6 M KOH solution. The potential range was between –1 to 0 V (Ag/AgCl) at different scan rates at the ambient temperature.

Impedance Measurements. Electrochemical impedance spectroscopic (EIS) measurements were performed under open circuit potential in an AC frequency range from 100,000 to 0.01 Hz with the excitation signal of 5 mV.

PPZS Spheres. TEA (2 mL) was added to a 300-mL round-bottom flask containing a mixture of HCCP (0.80 g), BPS (1.74 g) and acetonitrile (200 mL). The resulting mixture was supersonicated (200 W, 40 kHz) at 40 °C for 5 h. The precipitate was collected by centrifugation, washed three times with acetone and deionized water, and dried at 50 °C under vacuum for 24 h to give PPZS as a white powder in 92% yield.

TAPT-DHTA-COF. A mixture of mesitylene/dioxane (0.5 mL/0.5 mL), TAPT (28 mg), DHTA (20 mg), and aqueous acetic acid solution (3 M, 0.2 mL) in a Pyrex tube (10 mL) was degassed by three freeze-pump-thaw cycles. The tube was sealed off and heated at 120 °C for

3 days. The precipitate was collected by centrifugation, washed with THF, and dried at 120 °C under vacuum overnight to obtain TAPT-DHTA-COF in 86 % yield.

TAPT-DHTA-COF_x@PPZS. PPZS (30 mg for X = 0.05, 40 mg for X = 0.1, and 50 mg for X = 0.2) was dispersed in dioxane (0.5 mL) in a Pyrex tube (10 mL) and supersonicated for 10 min. The resulted mixture was added with TAPT (4.2 mg) and acetic acid (0.2 mL, 3 M), and was supersonicated for 10 min. DHTA (3 mg) in mesitylene (0.5 mL) was added to the tube, and the mixture was degassed by three freeze-pump-thaw cycles. After heating at 120 °C for 3 days, the mixture was cooled at room temperature and the precipitates were collected by centrifugation. The solid was washed with THF and dried at 120 °C under vacuum overnight, to yield TAPT-DHTA-COF_{0.2}@PPZS (35.7 mg), TAPT-DHTA-COF_{0.1}@PPZS (44.2 mg) and TAPT-DHTA-COF_{0.05}@PPZS (52.6 mg) as red powders.

PPZS₉₀₀, TAPT-DHTA-COF₉₀₀, and TAPT-DHTA-COF_x@PPZS₉₀₀. TAPT-DHTA-COF_x@PPZS (X = 0.05, 0.1, and 0.2; 300 mg), PPZS (300 mg), or TAPT-DHTA-COF (300 mg) samples were heated at a rate of 2 °C min⁻¹ up to 900 °C and kept at 900 °C for 3 h under N₂, to yield TAPT-DHTA-COF_x@PPZS₉₀₀ (X = 0.05; 63 mg, X = 0.1; 96 mg, X = 0.2; 102 mg), PPZS₉₀₀ (114 mg), and TAPT-DHTA-COF₉₀₀ (165 mg), respectively.

Section B. Supporting Figures

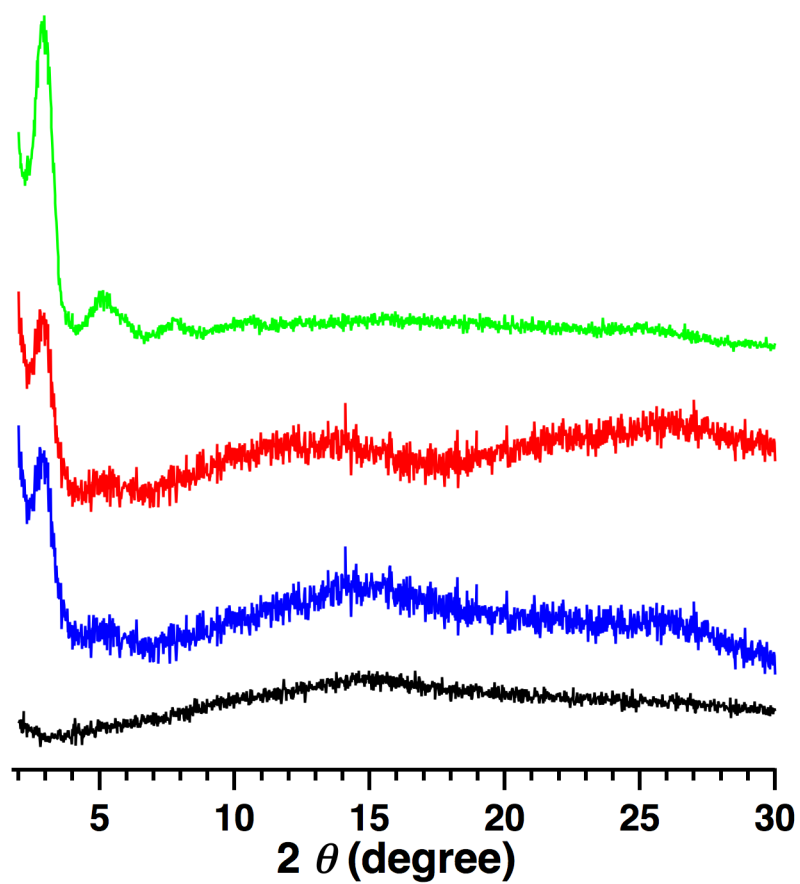


Figure S1. PXRD profiles of PPZS (black), TAPT-DHTA-COF_{0.05}@PPZS (blue), TAPT-DHTA-COF_{0.1}@PPZS (red), and TAPT-DHTA-COF_{0.2}@PPZS (green).

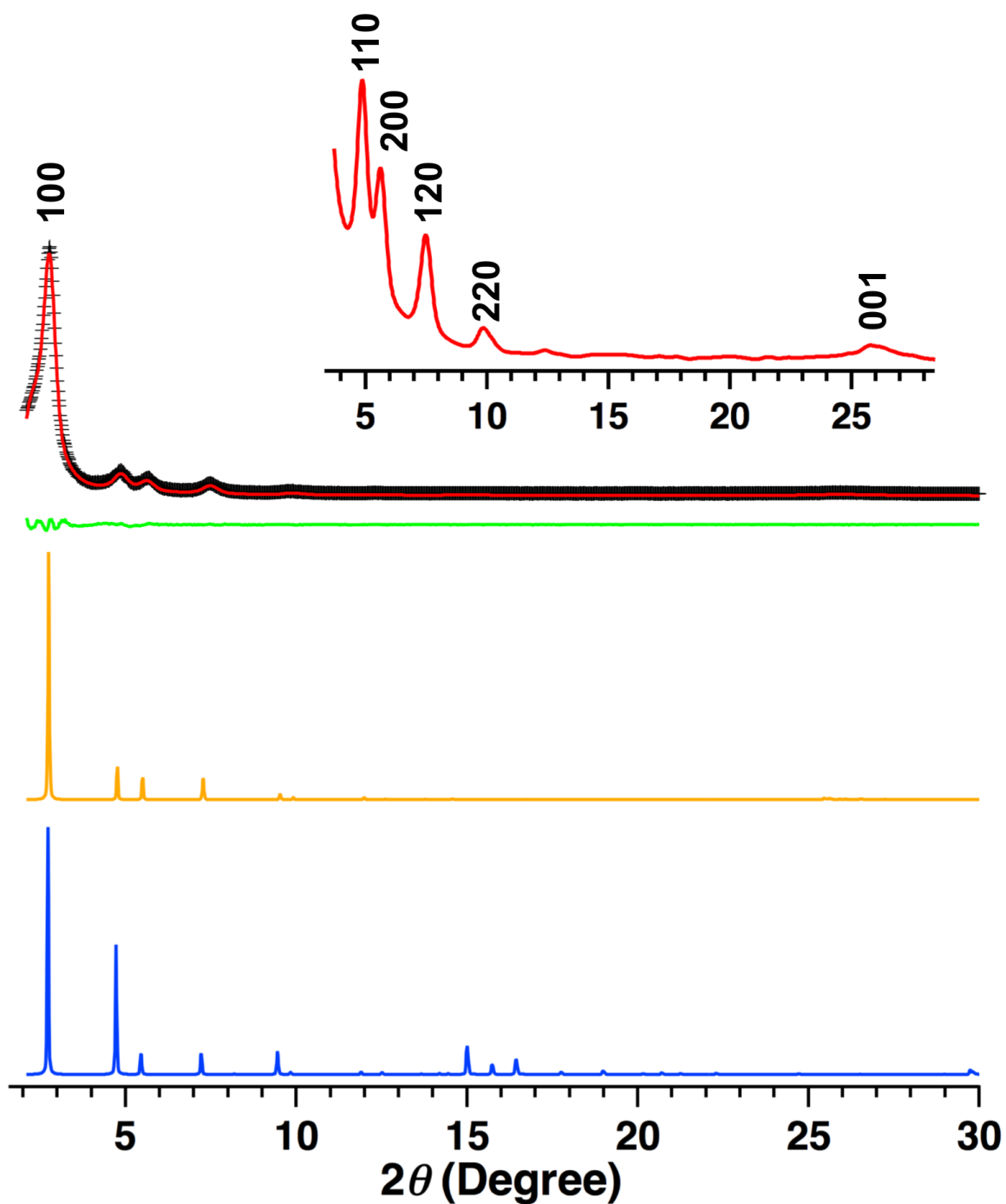


Figure S2. Indexed PXRD profiles of TAPT-DHTA-COF of the experimentally observed (red), the Pawley-refined (black), and their difference (green), the simulated using AA stacking model (orange) and AB stacking model (blue). $R_{WP} = 4.92\%$ and $R_P = 3.54\%$.

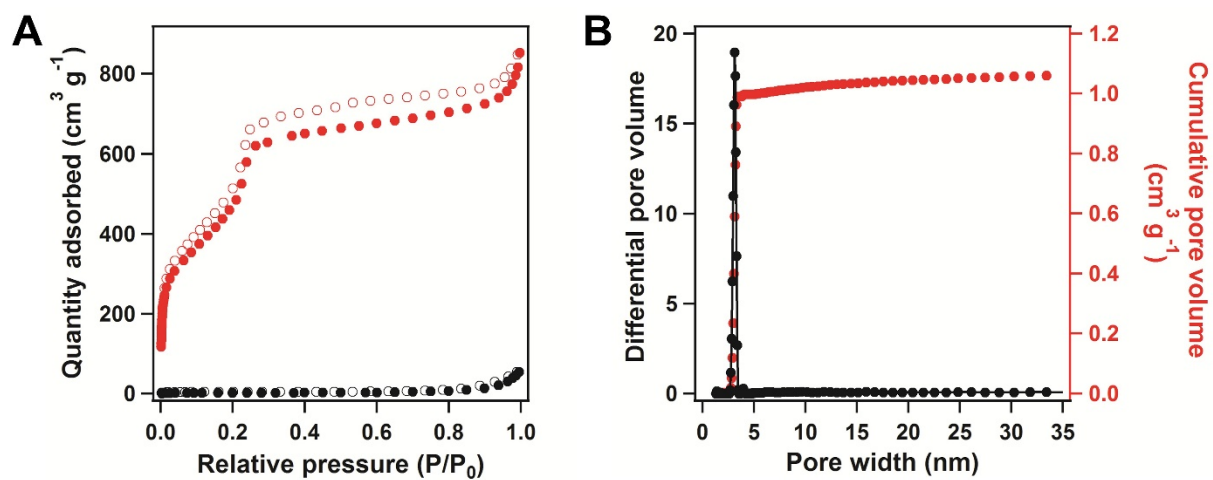


Figure S3. A) N₂ adsorption-desorption isotherms for TAPT-DHTA-COF (red) and TAPT-DHTA-COF₉₀₀ (black) at 77 K. B) Pore size distribution curve of TAPT-DHTA-COF.

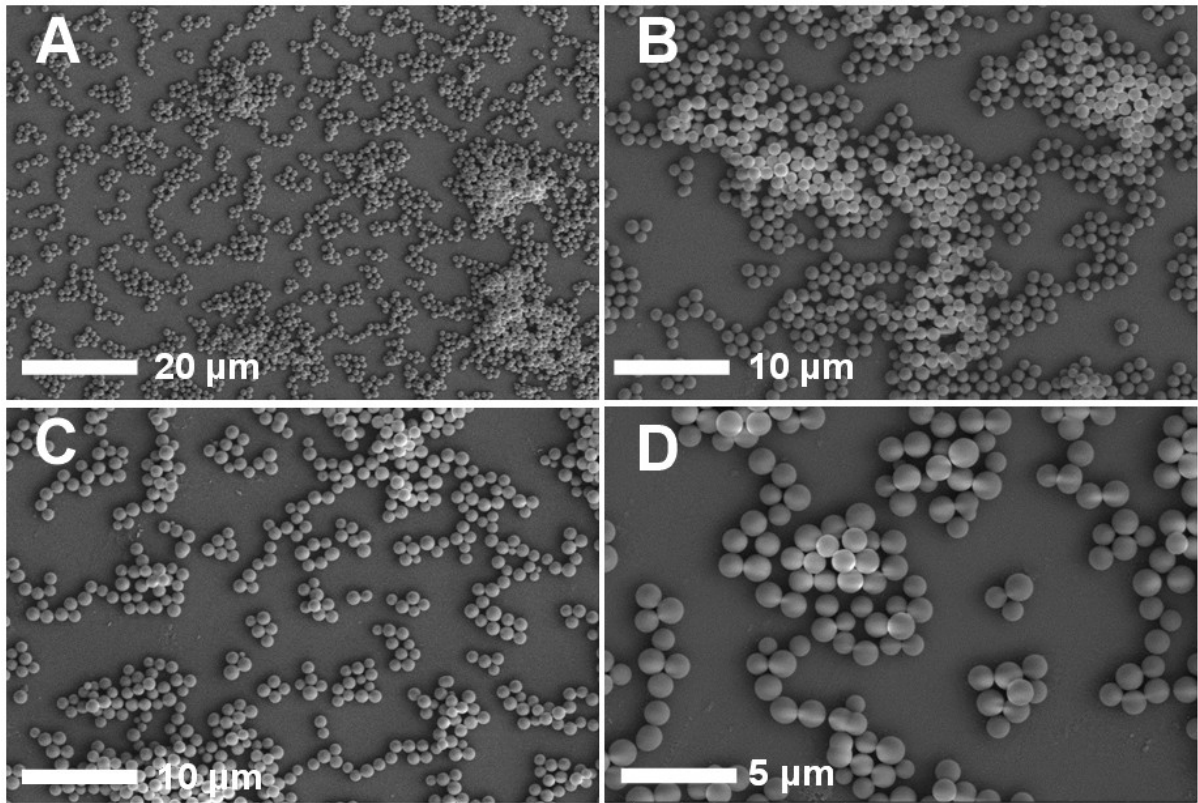


Figure S4. FE-SEM images of PPZS at different areas and magnifications.

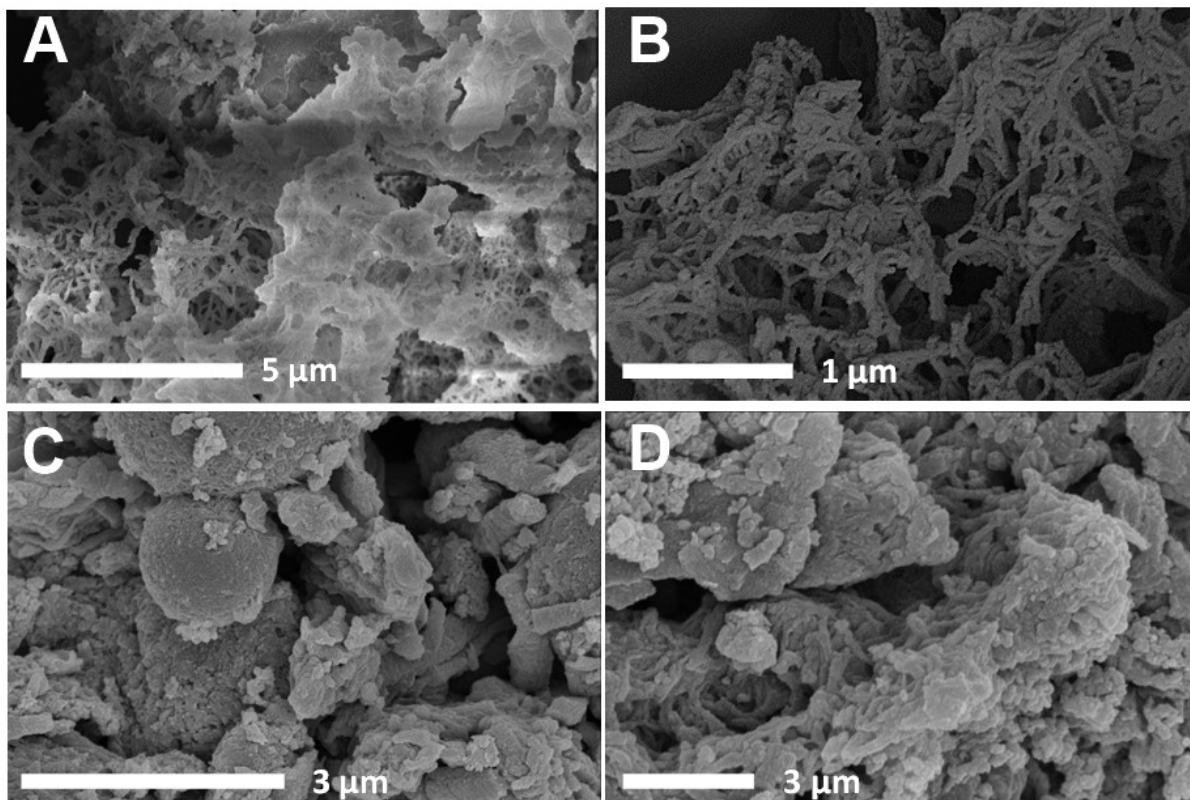


Figure S5. FE-SEM images of (A, B) TAPT-DHTA-COF and (C, D) TAPT-DHTA-COF₉₀₀. The shape was collapsed and the porosity disappeared upon direct pyrolysis (Figure S1A, black).

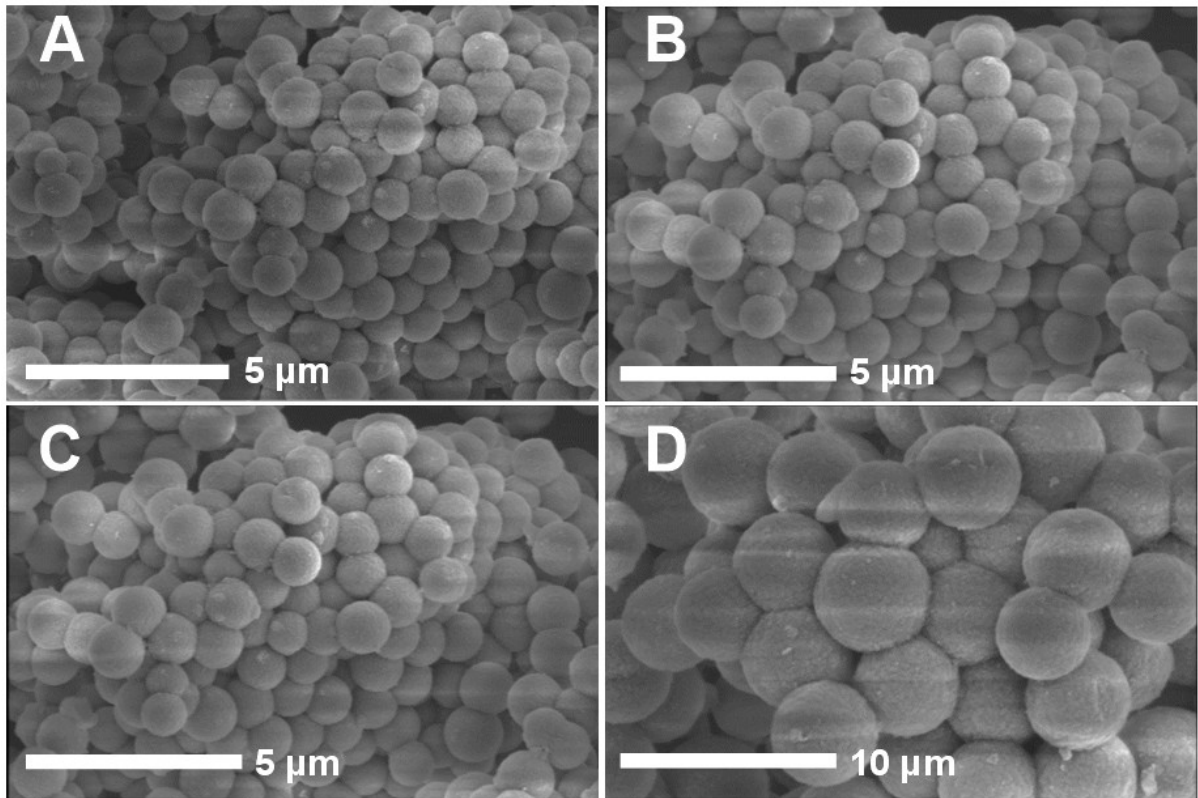


Figure S6. FE-SEM images of TAPT-DHTA-COF_{0.1}@PPZS at different areas and magnification scales.

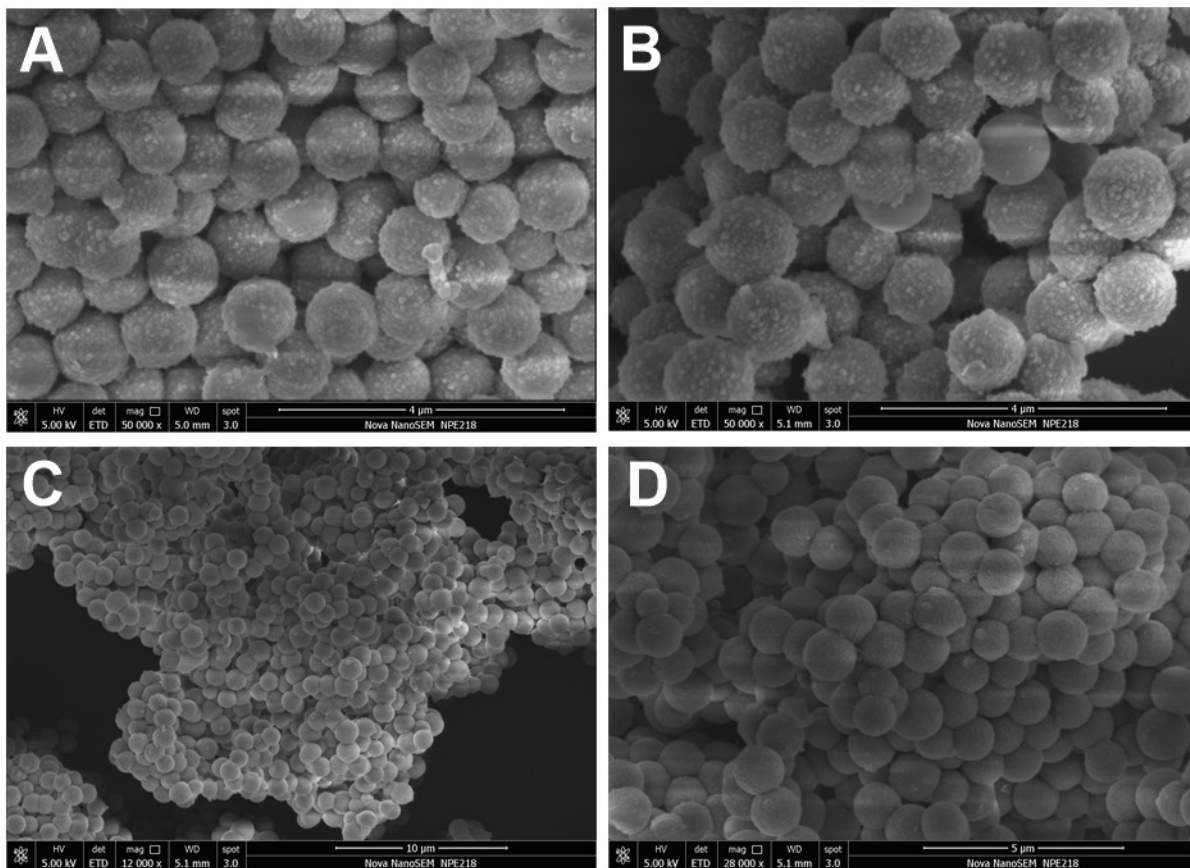


Figure S7. FE-SEM images of (A, B) TAPT-DHTA-COF_{0.2}@PPZS and (C, D) TAPT-DHTA-COF_{0.05}@PPZS at different areas and magnification scales.

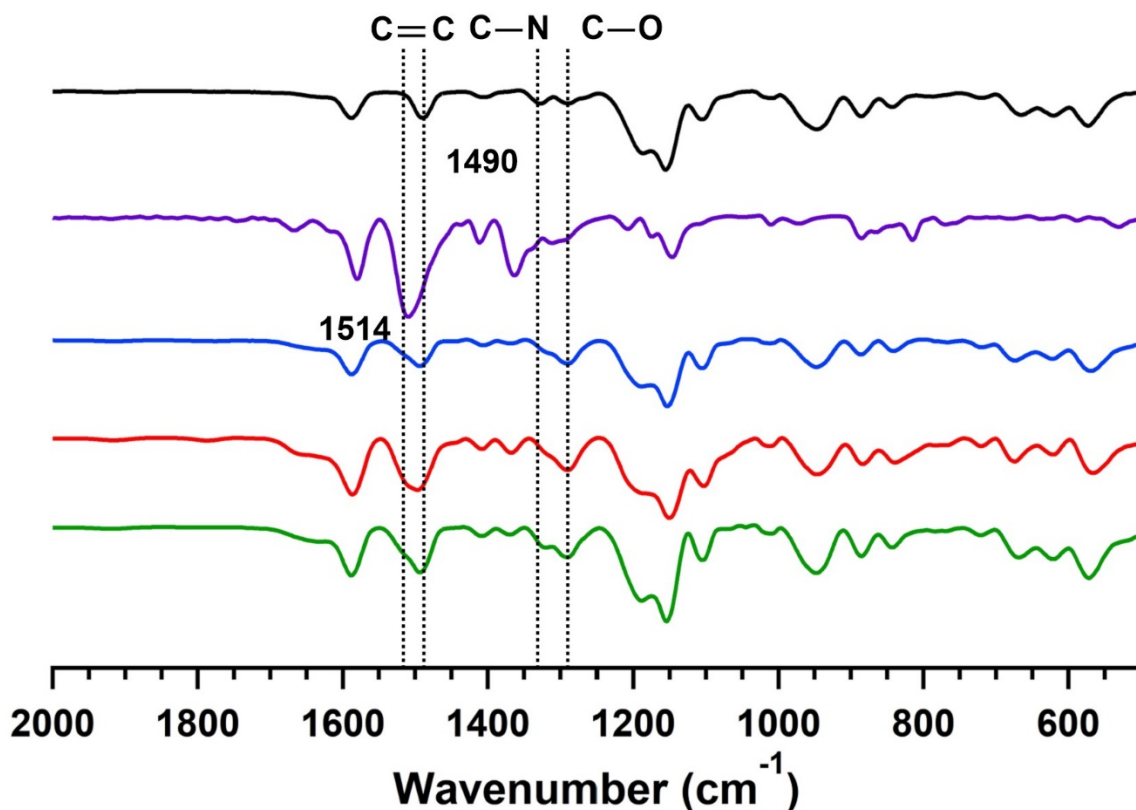


Figure S8. FT IR spectra of PPZS (black curve), TAPT-DHTA-COF (purple curve), TAPT-DHTA-COF_{0.05}@PPZS (blue curve), TAPT-DHTA-COF_{0.1}@PPZS (red curve) and TAPT-DHTA-COF_{0.2}@PPZS (green curve).

Infrared spectroscopy shows that the vibration band at 1490 cm⁻¹ observed for TAPT-DHTA-COF_x@PPZS is much broader than that of PPZS (Fig. S8, ESI[†]). This phenomenon originates from the combination of two bands in TAPT-DHTA-COF_x@PPZS; one at 1490 cm⁻¹ assigned to the phenyl C=C bond of PPZS, and another at 1514 cm⁻¹ assigned to the phenyl C=C bond of the COF skeleton. In addition, the intensity ratio between the bands at 1302 cm⁻¹ (C-O bond) and 1367 cm⁻¹ (C-N bond in triazine) was clearly enhanced for TAPT-DHTA-COF_x@PPZS.

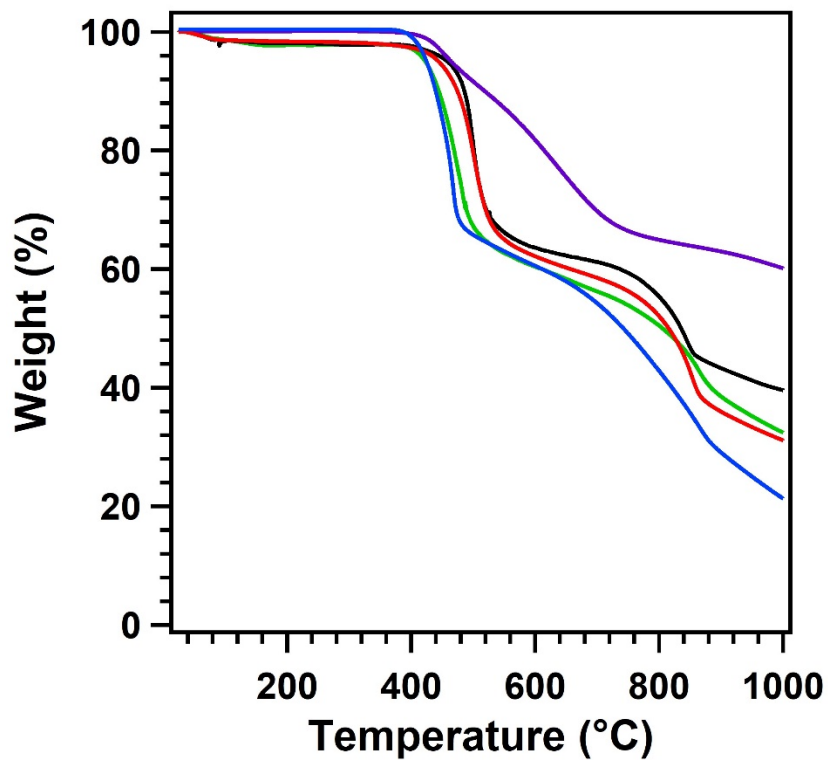


Figure S9. TGA curves of PPZS (black curve), TAPT-DHTA-COF (purple curve), TAPT-DHTA-COF_{0.05}@PPZS (blue curve), TAPT-DHTA-COF_{0.1}@PPZS (red curve) and TAPT-DHTA-COF_{0.2}@PPZS (green curve).

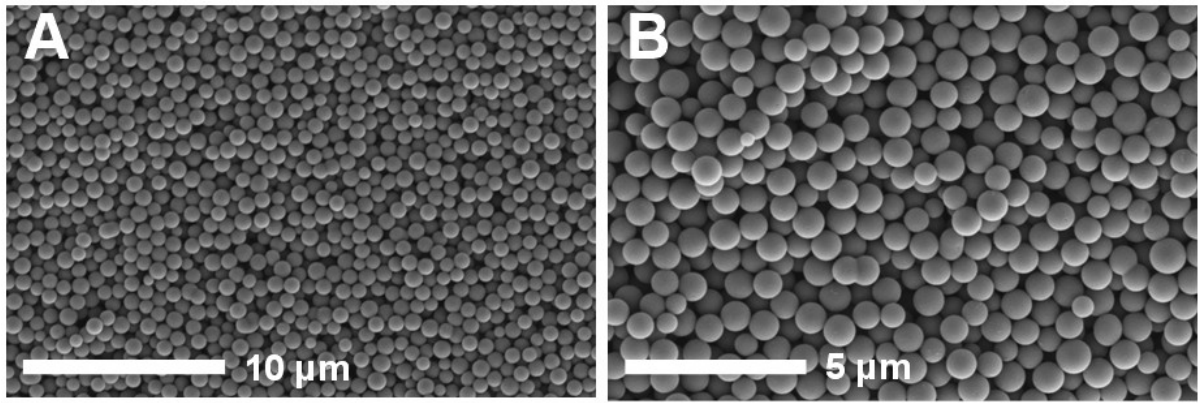


Figure S10. FE-SEM images of PPZS₉₀₀ at different magnification scales.

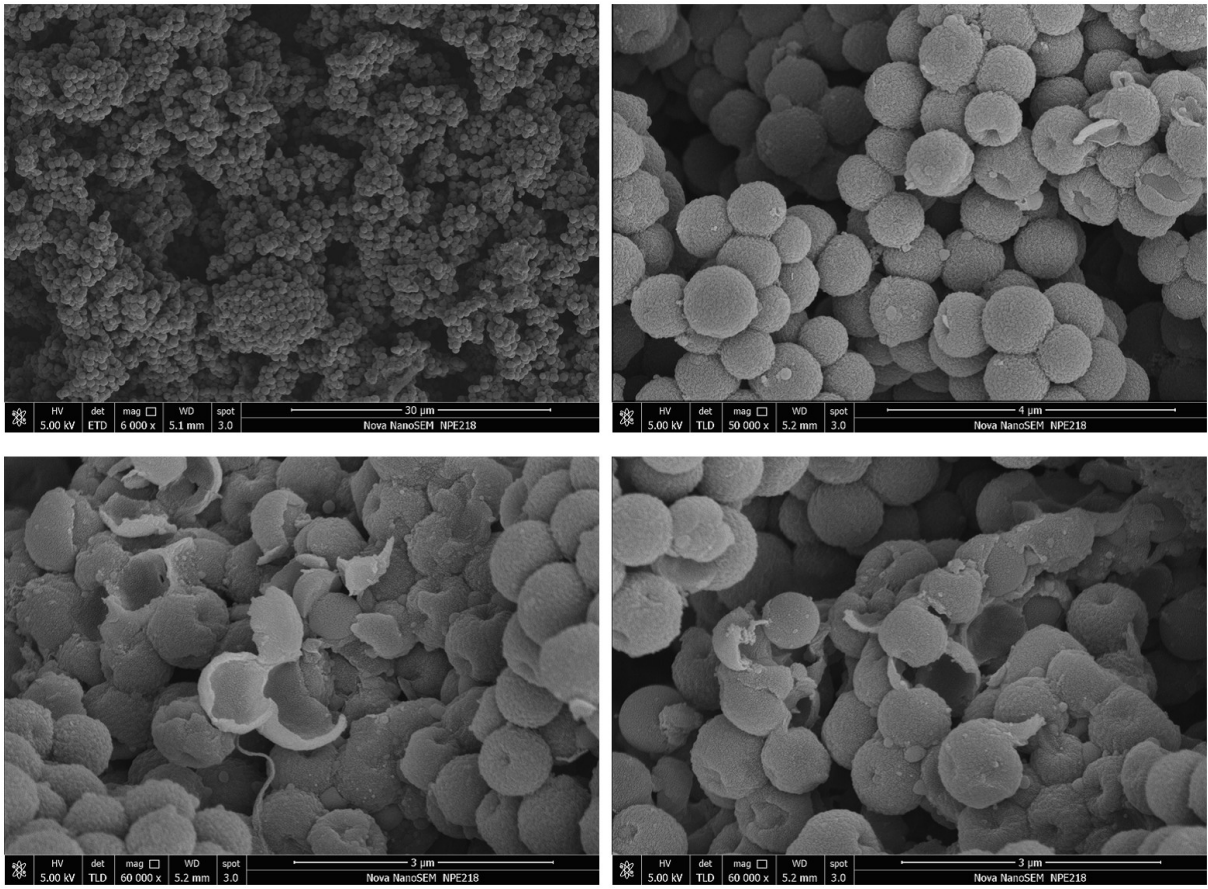


Figure S11. FE-SEM images of TAPT-DHTA-COF_{0.05}@PPZS₉₀₀ at different areas and magnification scales.

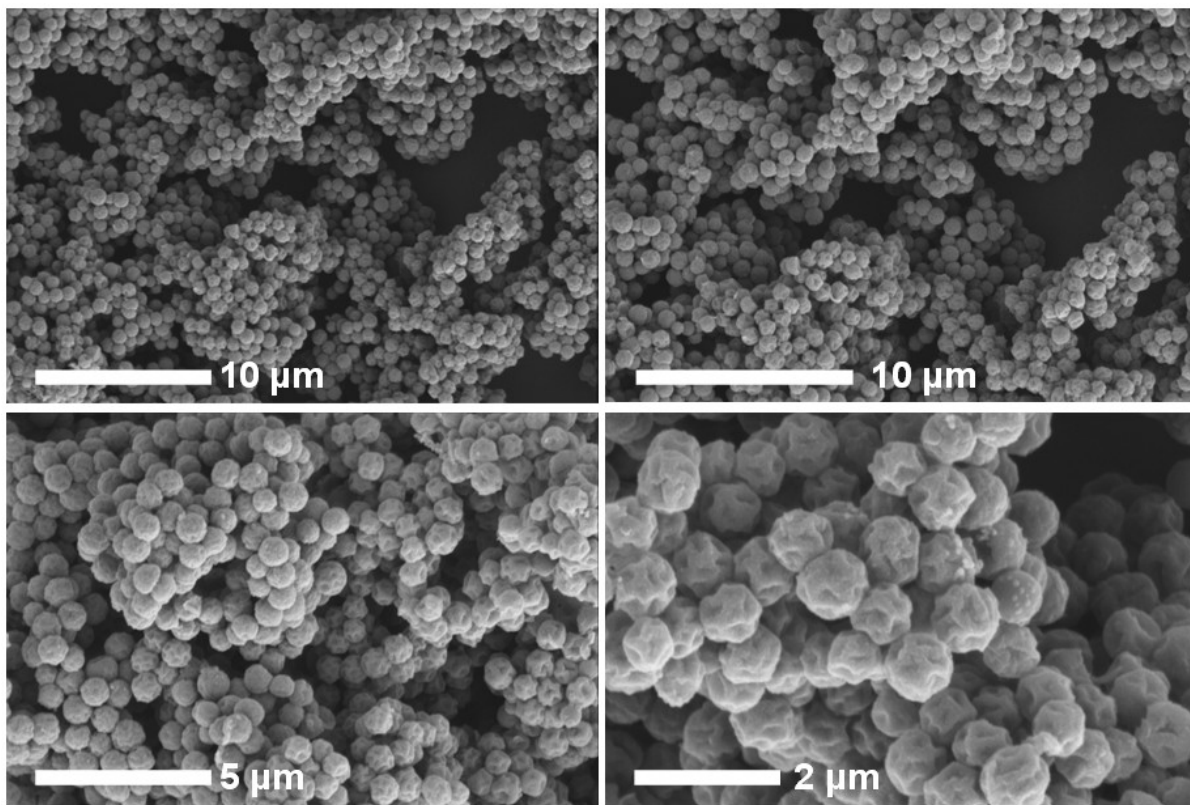


Figure S12. FE-SEM images of TAPT-DHTA-COF_{0.1}@PPZS₉₀₀ at different areas and magnification scales.

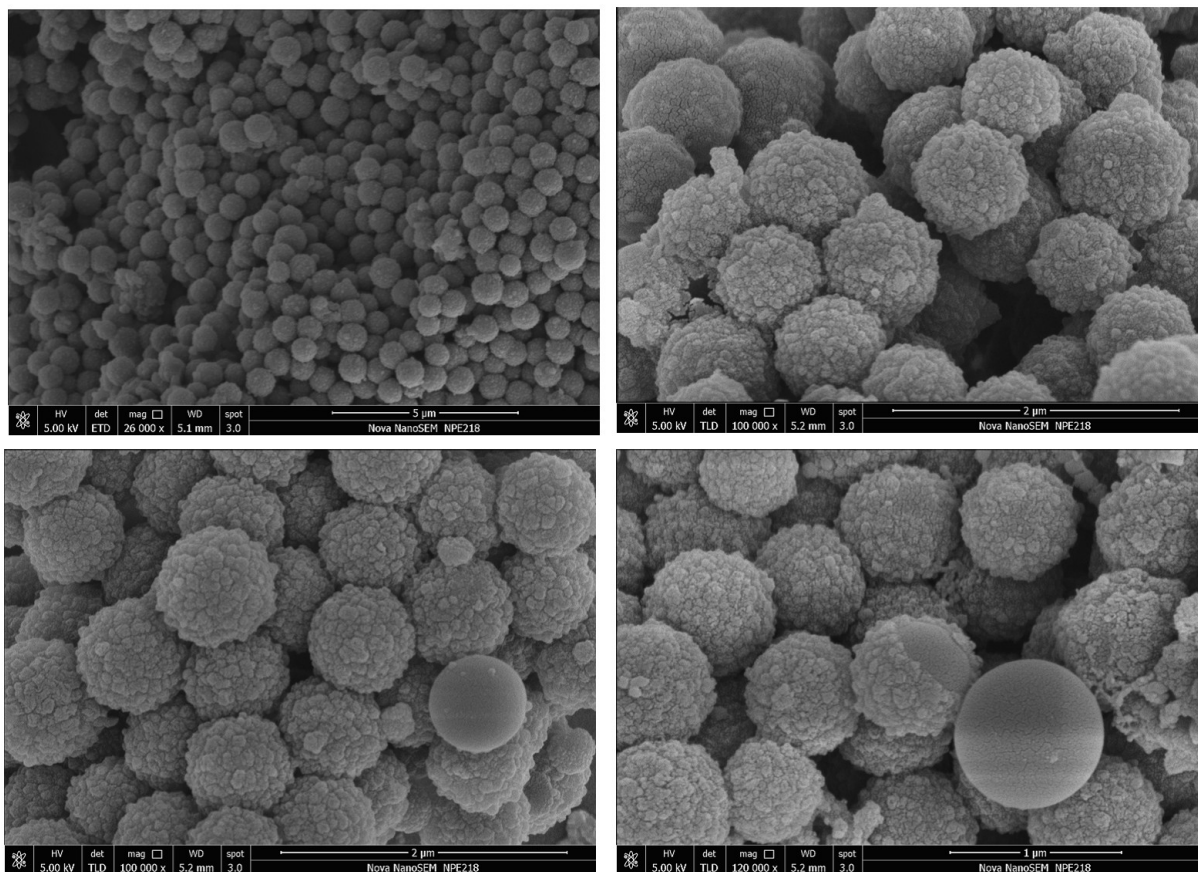


Figure S13. FE-SEM images of TAPT-DHTA-COF_{0.2}@PPZS₉₀₀ at different magnification scales.

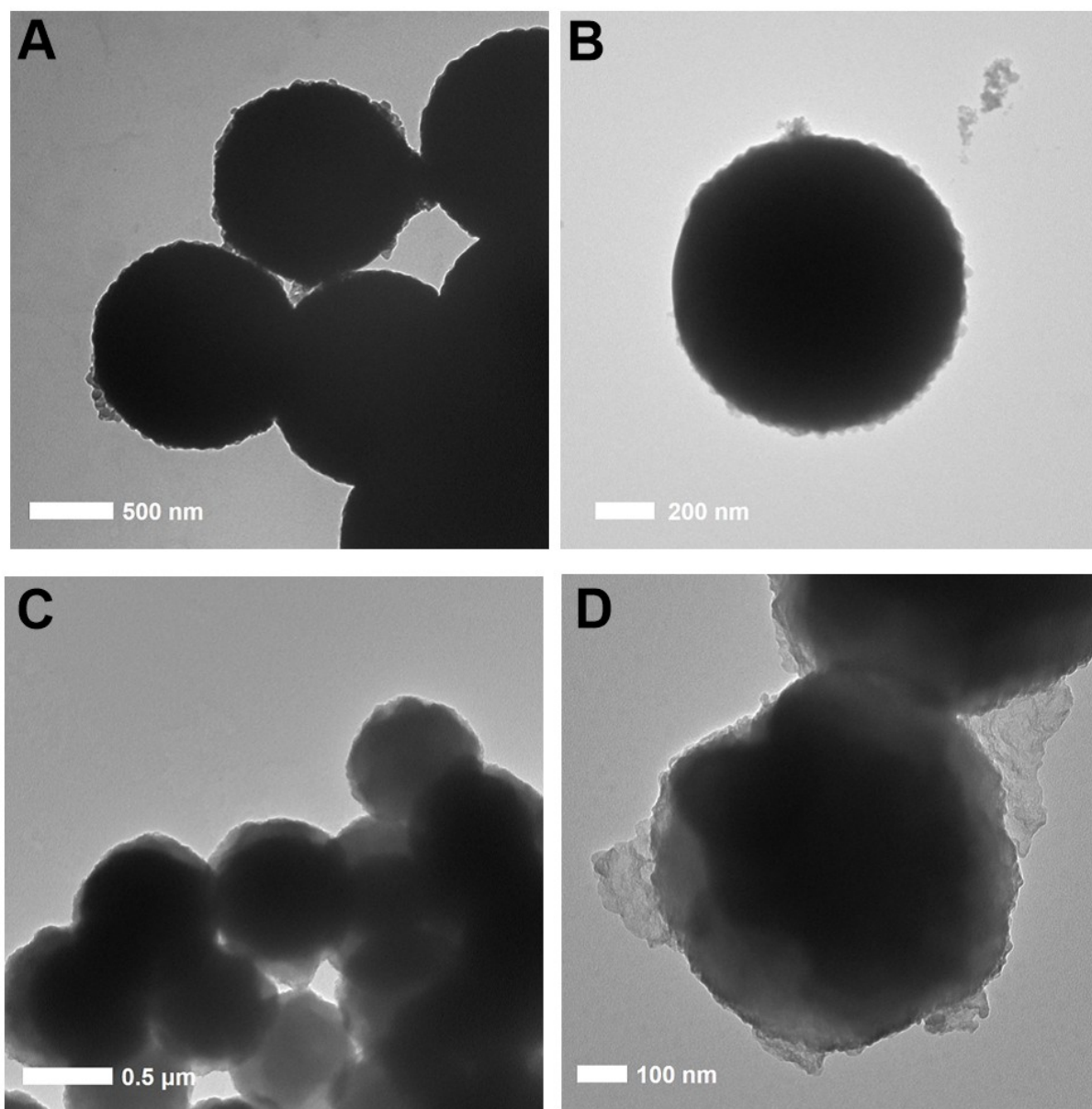


Figure S14. HR TEM images of (A, B) TAPT-DHTA-COF_{0.1}@PPZS and (C, D) TAPT-DHTA-COF_{0.1}@PPZS₉₀₀ at different magnifications.

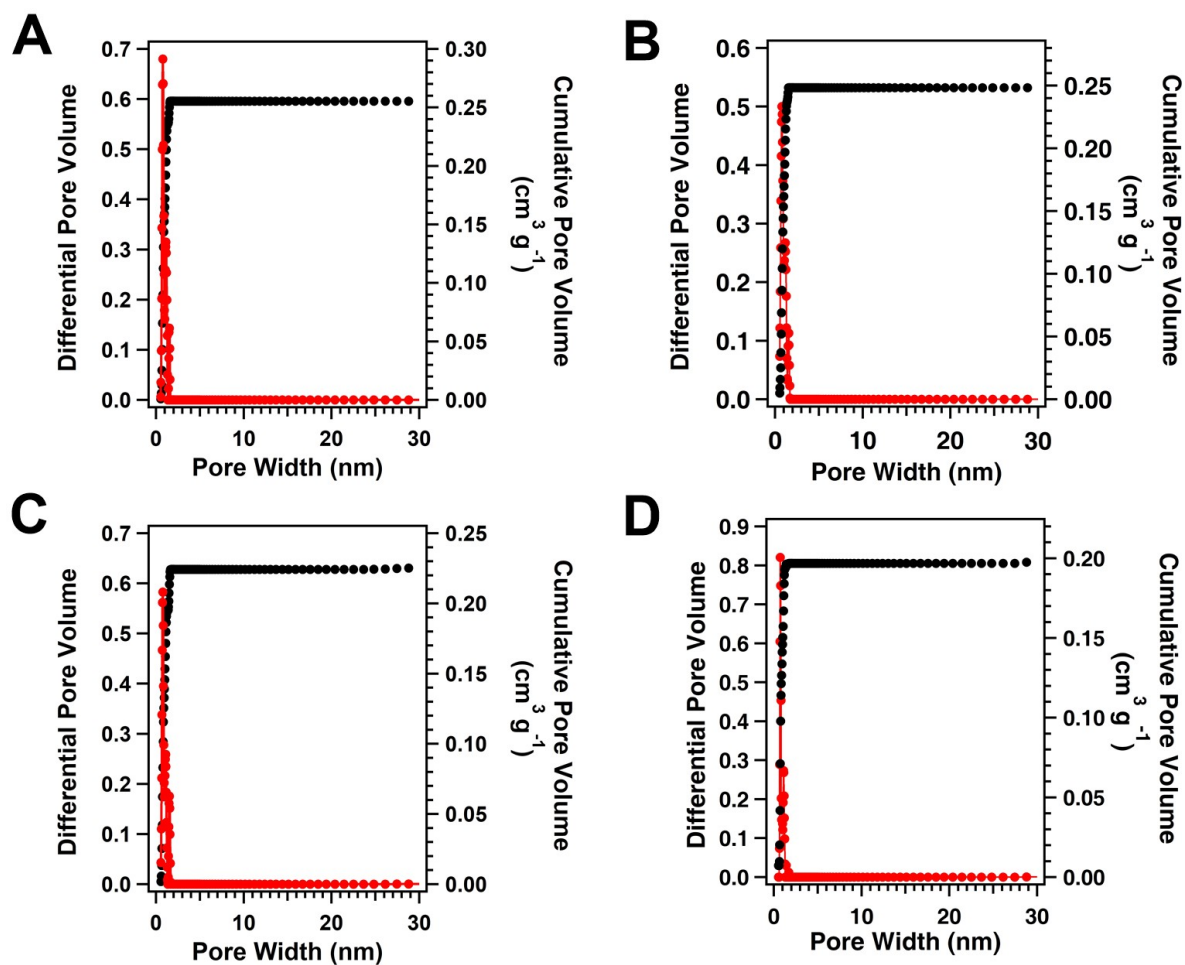


Figure S15. Pore size and distribution curves of (A) PPZS₉₀₀, (B) TAPT-DHTA-COF_{0.05}@PPZS₉₀₀, (C) TAPT-DHTA-COF_{0.1}@PPZS₉₀₀, and (D) TAPT-DHTA-COF_{0.2}@PPZS₉₀₀.

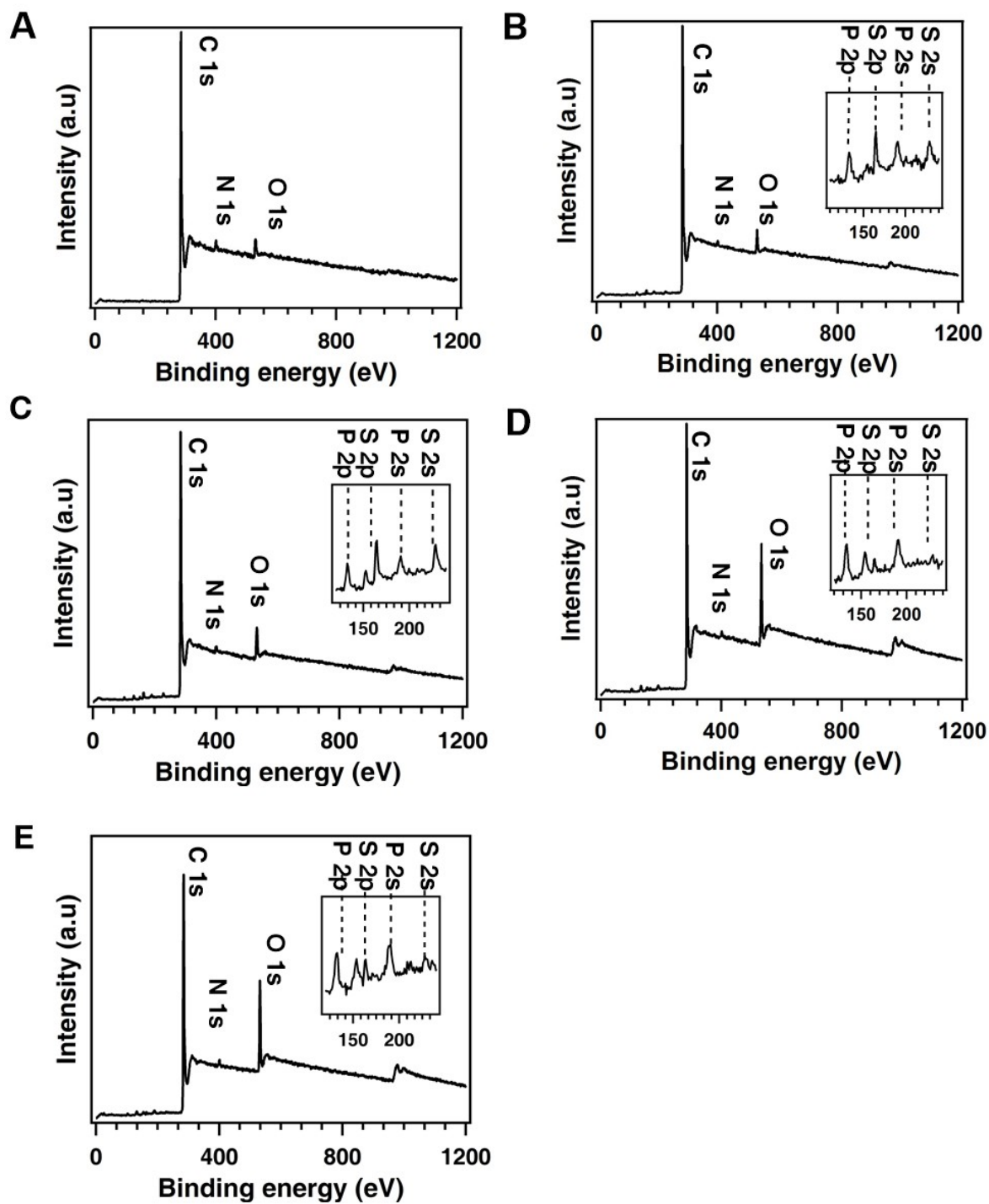


Figure S16. XPS profiles of (A) TAPT-DHTA-COF₉₀₀, (B) PPZS₉₀₀, (C) TAPT-DHTA-COF_{0.05}@PPZS₉₀₀, (D) TAPT-DHTA-COF_{0.1}@PPZS₉₀₀, and (E) TAPT-DHTA-COF_{0.2}@PPZS₉₀₀.

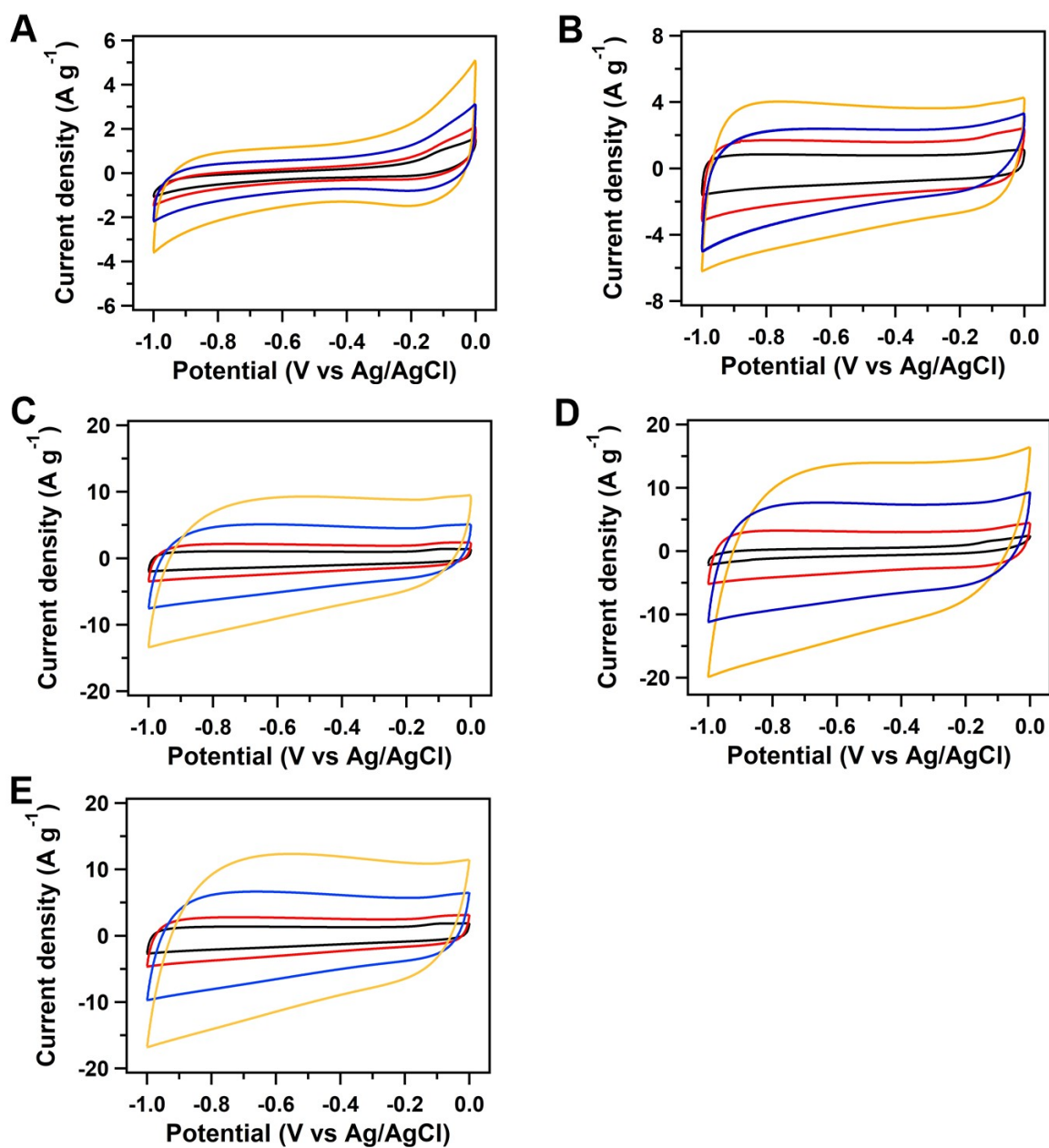


Figure S17. CV curves of (A) TAPT-DHTA-COF₉₀₀, (B) PPZS₉₀₀, (C) TAPT-DHTA-COF_{0.05}@PPZS₉₀₀, (D) TAPT-DHTA-COF_{0.1}@PPZS₉₀₀ and (E) TAPT-DHTA-COF_{0.2}@PPZS₉₀₀ at different scan rates of 10 (black), 20 (red), 50 (blue), and 100 mV s⁻¹ (yellow).

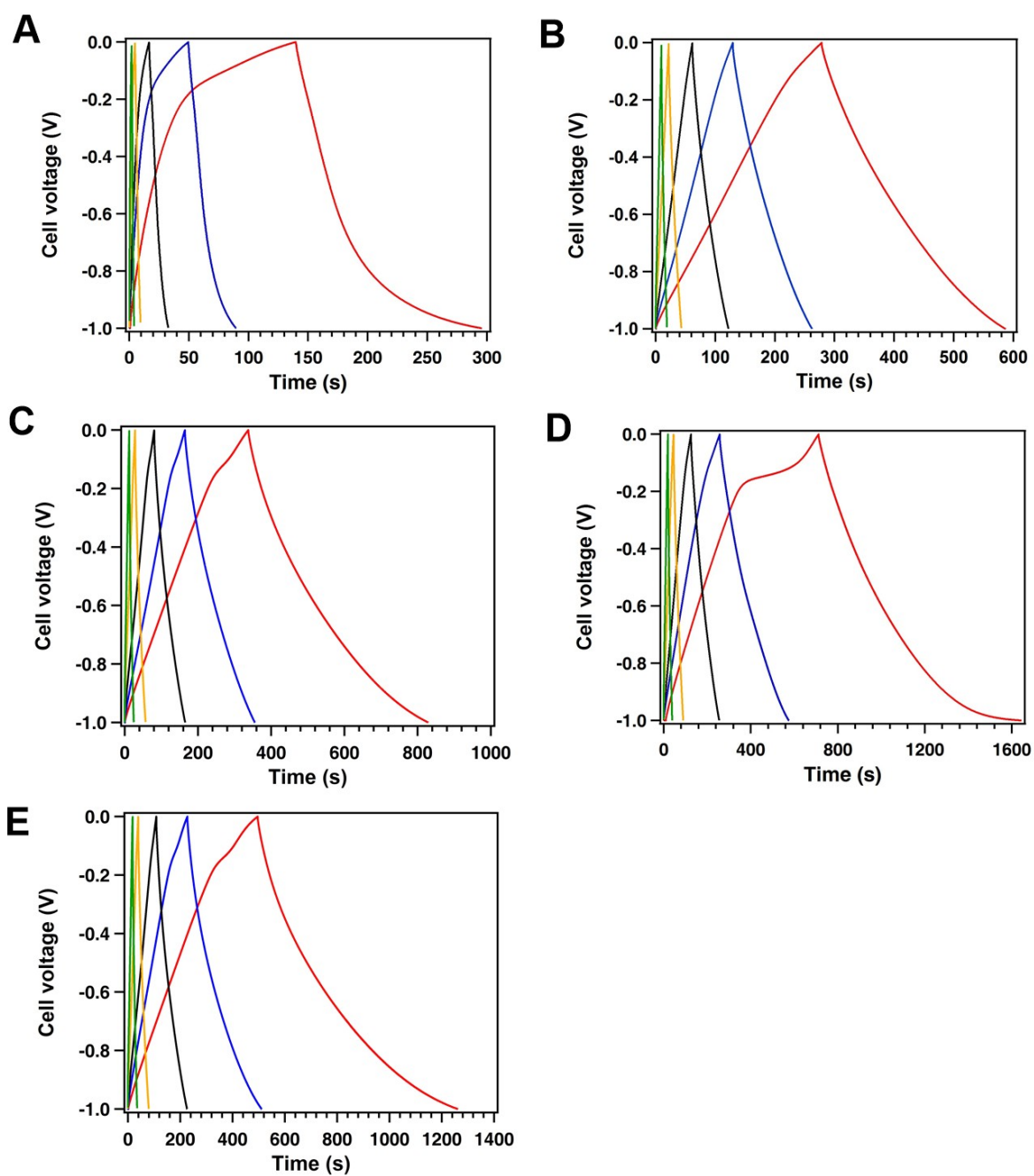


Figure S18. Galvanostatic charge-discharge curves of (A) TAPT-DHTA-COF₉₀₀, (B) PPZS₉₀₀, (C) TAPT-DHTA-COF_{0.05}@PPZS₉₀₀, (D) TAPT-DHTA-COF_{0.1}@PPZS₉₀₀, and (E) TAPT-DHTA-COF_{0.2}@PPZS₉₀₀ at different current densities of 0.5 (red), 1 (blue), 2 (black), 5 (yellow), and 10 A g⁻¹ (green).

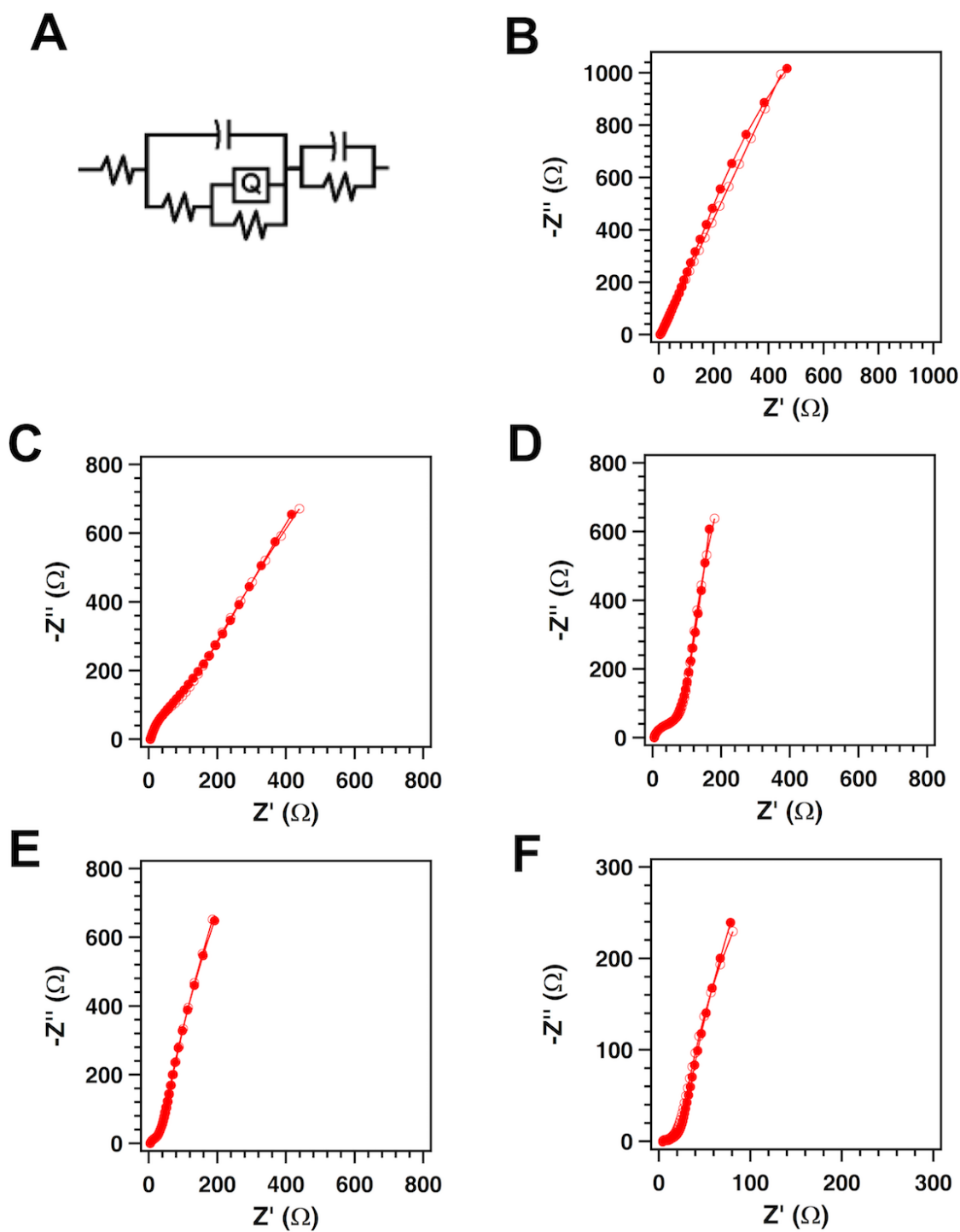


Figure S19. (A) Equivalent circuit of the supercapacitors. Impedance spectra of supercapacitors based on (B) TAPT-DHTA-COF₉₀₀, (C) PPZS₉₀₀, (D) TAPT-DHTA-COF_{0.05}@PPZS₉₀₀, (E) TAPT-DHTA-COF_{0.1}@PPZS₉₀₀, and (F) TAPT-DHTA-COF_{0.2}@PPZS₉₀₀ (filled dots are the experiment data and open dots are the simulated data).

Section C. Supporting Tables

Table S1. Pore structure of TAPT-DHTA-COF_{0.05}@PPZS, TAPT-DHTA-COF_{0.1}@PPZS, TAPT-DHTA-COF_{0.2}@PPZS, PPZS₉₀₀, TAPT-DHTA-COF_{0.05}@PPZS₉₀₀, TAPT-DHTA-COF_{0.1}@PPZS₉₀₀, and TAPT-DHTA-COF_{0.2}@PPZS₉₀₀.

Samples	BET surface areas (m² g⁻¹)	Pore volume (cm³ g⁻¹)
TAPT-DHTA-COF_{0.05}@PPZS	57	0.028
TAPT-DHTA-COF_{0.1}@PPZS	156	0.065
TAPT-DHTA-COF_{0.2}@PPZS	290	0.147
PPZS₉₀₀	607	0.26
TAPT-DHTA-COF_{0.05}@PPZS₉₀₀	533	0.25
TAPT-DHTA-COF_{0.1}@PPZS₉₀₀	456	0.22
TAPT-DHTA-COF_{0.2}@PPZS₉₀₀	421	0.2

Table S2. Elemental contents of PPZS₉₀₀, TAPT-DHTA-COF₉₀₀, TAPT-DHTA-COF_{0.05}@PPZS₉₀₀, TAPT-DHTA-COF_{0.1}@PPZS₉₀₀, and TAPT-DHTA-COF_{0.2}@PPZS₉₀₀ according to the XPS analysis.

Samples	C at%	O at%	N at%	S at%	P at%
TAPT-DHTA-COF₉₀₀	95.92	2.17	1.91	0	0
PPZS₉₀₀	94.34	3.02	1.55	0.4	0.7
TAPT-DHTA-COF_{0.05}@PPZS₉₀₀	92.63	3.91	2.02	0.79	0.64
TAPT-DHTA-COF_{0.1}@PPZS₉₀₀	87.79	9.64	1.37	0.21	0.99
TAPT-DHTA-COF_{0.2}@PPZS₉₀₀	87.62	9.89	1.29	0.23	0.97

Table S3. Capacitances of TAPT-DHTA-COF_{0.1}@PPZS₉₀₀, COF-based materials, and state-of-the-art carbon materials.

Carbons	Electrolyte	Current Density	Capacitance (F g ⁻¹)	Reference
TAPT-DHTA-COF_{0.1}@PPZS₉₀₀	6 M KOH	1 A/g 0.5 A/g	287 411	This work
GNrib	1 M H ₂ SO ₄	1 A/g	168	<i>Nat. Chem.</i> 2016 , 8, 718-724.
HPG	0.5 M H ₂ SO ₄	0.5 A/g	225	<i>ACS Cent. Sci.</i> 2015 , 1, 68-76.
NPC-F	6 M KOH	1 A/g	284	<i>Adv. Mater.</i> 2016 , 28, 1981-1987.
Graphene (activated)	BMIM ₄ /AN	0.7 A/g	200	<i>Science</i> 2011 , 332, 1537-1541.
Lasers Cribbed Graphene	1 M H ₂ SO ₄	1 A/g	202	<i>Science</i> 2012 , 335, 1326-1330.
Hierarchical Carbon Material	6 M KOH	175 mA/g	198	<i>Energy Environ. Sci.</i> 2011 , 4, 4504-4507.
HMCNs-180	2 M H ₂ SO ₄	5 mV/s	95	<i>Nano Lett.</i> 2013 , 13, 207-212.
Carbon-L-950	6 M KOH	0.1 A/g	228	<i>Adv. Mater.</i> 2014 , 26, 2047-2051.
CM-NF	6 M KOH	0.1 A/g	189	<i>Nat. Commun.</i> 2015 , 6, 8503.
PTF-700	EMIMBF ₄	0.1 A/g	151.3	<i>J. Am. Chem. Soc.</i> 2015 , 137, 219-225.
GNF	EMIMBF ₄	0.5 A/g	193	<i>J. Am. Chem. Soc.</i> 2014 , 136, 2256-2259.
GCA	6 M KOH	1 A/g	180	<i>Sci. Rep.</i> 2016 , 6, 3154.
PAF-Carbon	1 M H ₂ SO ₄	0.5 A/g	173	<i>Sci. Rep.</i> 2015 , 5, 8307.
NCCFs	6 M KOH	1 A/g	240	<i>Sci. Rep.</i> 2015 , 5, 15388.

DAAQ-TFP COFs	1 M H ₂ SO ₄	0.1 A/g	40	<i>J. Am. Chem. Soc.</i> , 2013 , 135, 16821.
(TEMPO)_{100%}-NiP-COF	(C ₄ H ₉) ₄ ClO ₄	2 A/g	113	<i>Angew. Chem. Int. Ed.</i> , 2015 , 54, 6814.
TaPa-Py COF	1 M H ₂ SO ₄	0.5 A/g	209	<i>J. Mater. Chem. A</i> , 2016 , 4, 16312.
NH₂-f-MWCNT@COF_{TTA-DHTA}	1 M Na ₂ SO ₄	0.4 A/g	127.5	<i>Chem. Commun.</i> , 2017 , 53, 6303.

Section D. References

[S1] B. Aradi, B. Hourahine, T. Frauenheim, *J. Phys. Chem. A* **2007**, *111*, 5678-5684.

[S2] <http://www.dftb.org>.